SISSA

Design and performance characterisation of the HAPG von Hámos Spectrometer at the High Energy Density Instrument of the European XFEL

View the article online for updates and enhancements.

You may also like

Design and performance characterisation of the HAPG von Hámos Spectrometer at the High Energy Density Instrument of the European XFEL

T.R. Preston,[a,1] **S. Göde,**[a] **J.-P. Schwinkendorf,**[a] **K. Appel,**[a] **E. Brambrink,**[a] **V. Cerantola,**[a] **H. Höppner,**[b] **M. Makita,**[a] **A. Pelka,**[b] **C. Prescher,**[c] **K. Sukharnikov,**[a] **A. Schmidt,**[a] **I. Thorpe,**[a] **T. Toncian,**[b] **A. Amouretti,**[d] **D. Chekrygina,**[b] **R.W. Falcone,**[e] **K. Falk,**[b,f,g] **L.B. Fletcher,**[h] **E. Galtier,**[h] **M. Harmand,**[d] **N.J. Hartley,**[b,h] **S.P. Hau-Riege,**[i] **P. Heimann,**[h] **L.G. Huang,**[b] **O.S. Humphries,**[j] **O. Karnbach,**[j] **D. Kraus,**[b,k] **H.J. Lee,**[h] **B. Nagler,**[h] **S. Ren,**[j] **A.K. Schuster,**[b,f] **M. Smid,**[b] **K. Voigt,**[b] **M. Zhang**[b] **and U. Zastrau**[a]

[a] *European XFEL,*
Holzkoppel 4, 22869 Schenefeld, Germany

[b] *Helmholtz-Zentrum Dresden-Rossendorf,*
Bautzner Landstr. 400, 01328 Dresden, Germany

[c] *Deutsches Elektronen-Synchrotron DESY,*
Notkestr. 85, 22607 Hamburg, Germany

[d] *Institut de Minéralogie, de Physique des Matériaux, et de Cosmochimie (IMPMC), Sorbonne Université,*
UMR CNRS 7590, Muséum National d'Histoire Naturelle,
75005 Paris, France

[e] *Department of Physics, University of California,*
Berkeley, California 94720, U.S.A.

[f] *Technische Universität Dresden,*
01069 Dresden, Germany

[g] *Institute of Physics of the ASCR,*
182 21 Prague, Czech Republic

[h] *SLAC National Accelerator Laboratory,*
2575 Sand Hill Road, Menlo Park, California 94025, U.S.A.

[i] *Lawrence Livermore National Laboratory,*
7000 East Avenue, Livermore, California 94550, U.S.A.

[j] *Department of Physics, Clarendon Laboratory, University of Oxford,*
Parks Road, Oxford OX1 3PU, United Kingdom

[k] *Institut für Physik, Universität Rostock,*
Albert-Einstein-Str. 23, 18059 Rostock, Germany

E-mail: thomas.preston@xfel.eu

---

[1]Corresponding author.

ABSTRACT: The von Hámos spectrometer setup at the HED instrument of the European XFEL is described in detail. The spectrometer is designed to be operated primarily between 5 and 15 keV to complement the operating photon energy range of the HED instrument. Four Highly Annealed Pyrolitic Graphite (HAPG) crystals are characterised with thicknesses of 40 μm or 100 μm and radius-of-curvature 50 mm or 80 mm, in conjunction with either an ePix100 or Jungfrau detector. The achieved resolution with the 50 mm crystals, operated between 6.5 and 9 keV, matches that reported previously: ∼ 8 eV for a thickness of 40 μm, whereas, with an 80 mm crystal of thickness 40 μm, the resolution exceeds that expected. Namely, a resolution of 2 eV is demonstrated between 5–6 keV implying a resolving power of 2800. Therefore, we posit that flatter HAPG crystals, with their high reflectivity and improved resolving power, are a powerful tool for hard x-ray scattering and emission experiments allowing unprecedented measurements of collective scattering in a single shot.

Contents

1 Introduction

Spectrally resolved measurements of x-rays scattered from or emitted by a sample are an important technique for diagnosing high energy density matter. In particular, with an energy resolution of order a few eV, non-collective Compton scattering [1], collective plasmon scattering [2], and bound-free scattering provide information about the electronic sub-system, such as its temperature and density [3], internal energy levels [4], and the dielectric function [5]. Cylindrically bent crystals, exploiting mosaic focusing in von Hámos geometry [6], therefore offer a compelling choice for experiments that require high reflectivity and modest resolving power and have been previously characterised at length for variants of Highly Oriented Pyrolitic Graphite (HOPG) [7] and Highly Annealed Pyrolitic Graphite (HAPG) [8]. Alternative concepts without mosaic focusing include perfect, bent crystals of GaAs [9], and segmented Si crystals [10] operated at high Bragg angles. These crystals have been used to enable measurements of Thomson scattering [11], and thereby elucidate plasmon dispersions [2, 3, 12, 13] and further measurements of transport [5] and optical properties [14] of warm-dense matter, amongst others. Often, these measurements require a discernable signal, even for a single shot, in optical-laser driven plasmas which discounts the use of less-reflective single crystal spectrometers [12, 13]. Furthermore, in cases where a high signal-to-noise ratio is desired, due to plasma background emission or EMP readout artefacts on the detector, focusing spectrometers are preferred where the spectrum is concentrated into a line. To facilitate future experiments, a flexible and powerful spectrometer setup has been designed and implemented at the High Energy Density (HED) instrument of the European X-ray Free Electron Laser (XFEL). The instrument's remit is to combine ultrashort ($\sim 10\,\mathrm{fs}$) high-brightness ($> 1\,\mathrm{mJ}$) state-of-the-art FEL-generated hard x-rays (5 to 25 keV) with a suite of drivers, for example the Helmholtz International Beamline for Extreme Fields (HIBEF) high-intensity and high-energy lasers, in order to attain extreme states of matter. Future developments at the HED instrument will include self-seeding which should reduce the x-ray bandwidth down from $\sim 20\,\mathrm{eV}$ for SASE (Self-Amplified Spontaneous Emission) to $\sim 1\,\mathrm{eV}$ for self-seeded emission enabling high-quality spectrum measurements in a single pulse, without recourse to monochromators which introduce transmission losses.
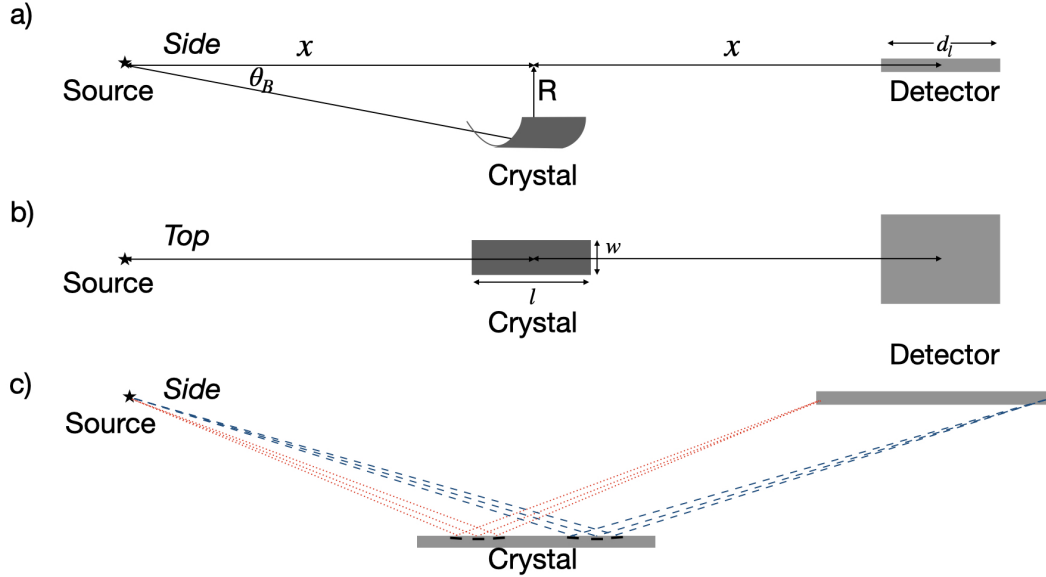
2 Conceptual design

Figure 1. Schematic setup of a spectrometer in von Hámos geometry viewed from the side a) and from the top b). The crystal is located at a linear distance x from the source, as is the detector from the crystal. The cylindrically bent crystal is offset from the source-detector ($2x$) line by its radius-of-curvature (R) making a Bragg angle of θ_B to the source-detector line resulting in focussing in the non-dispersive axis. The crystal has a width w and a length along its cylinder axis of l. The detector chip has length along the dispersive direction of d_l. Also shown in c) is an example of mosaic focussing (not to scale) viewed from the side: red dotted is the lowest energy recorded on the detector and blue dashed is the highest energy.

The spectrometer design must fulfill many competing criteria: it should flexibly cover a large range of photon energies, corresponding to the HED beam parameters, and coincide well with space considerations of other diagnostics, without restricting their line-of-sight to the target, or reducing its collection efficiency. An excellent and proven design [8] is based on the use of a cylindrically bent mosaic crystal in von Hámos geometry [6] with a 2D area detector operating in direct x-ray photon detection and with its chip oriented along the central cylinder axis.

A mosaic crystal comprises many small perfect crystallite domains of micrometre and submicrometre size [7, 15] which are oriented almost parallel to each other. The mosaic crystals are made from low-Z materials which have a low photoabsorption cross-section, meaning that rays that don't fulfill the Bragg condition at the surface can penetrate and be reflected from deeper layers allowing an increase of reflectivity with crystal thickness, with the downside of a possible increase in depth broadening depending on Bragg angle. Here we choose crystals made from different types of artificial graphite: either HOPG or HAPG with a $2d$ spacing for the (002) reflection of 6.708 Å. HOPG crystals have a mosaic spread [7] of order 0.4° for thicknesses of 100 μm, whereas HAPG crystals provide a smaller [8] mosaic spread (∼ 0.14°) but with comparably higher energy resolution, offset by a relatively lower reflectivity compared with HOPG. The integrated reflectivity

Table 1. Design parameters for the spectrometer with (002) reflection for source-to-crystal distance (x), crystal radius-of-curvature (R), central Bragg angle (θ_B), central reflected photon energy (E_C), spectral window for both ePix (ΔE_E) and Jungfrau (ΔE_J) detectors with their long axis aligned with the dispersive direction, and their pixel-normalised dispersions (dE/dx) for the central Bragg angle.

x (mm)	R (mm)	θ_B (°)	E_C (keV)	ΔE_E (eV)	ΔE_J (eV)	dE_E/dx (eV/pixel)	dE_J/dx (eV/pixel)
200	80	22	5.0	410	820	0.54	0.80
400	80	11	9.4	440	870	0.57	0.85
200	50	14	7.6	690	1380	0.90	1.35
400	50	7	14.9	700	1410	0.92	1.38

(product of peak reflectivity and rocking curve width) for a mosaic HAPG crystal is nevertheless large compared with perfect crystals and is ~ 1–2 mrad [8].

For successful mosaic focusing without blurring, the source-to-crystal and crystal-to-detector distances should be equal. This, combined with the cylindrical geometry, results in one-to-one focussing in the non-dispersive direction of the source onto the detector plane, as shown in figure 1, and subsequent resolving powers [8] of order $E/\Delta E \sim 500$–2000, enabling a range of uses from emission spectroscopy to inelastic x-ray scattering. The resolving power achieved depends on the source-size, photon energy and Bragg angle θ, which determines the depth broadening. In order to minimise depth broadening, which varies as $t/\sin(\theta)$, with t the crystal thickness and increases with shallower angles, the Bragg angle of the reflection should be kept above $\sim 10°$. Here the path length of a diffracted ray through the crystal remains less than the attenuation length. To coincide with space considerations in the HED interaction chamber (IC1), the source-to-crystal distance (x) is constrained to be between 200 and 400 mm, with a resulting crystal radius-of-curvature (R) ~ 50–80 mm. Two detectors will be considered here, the ePix100 [16] and Jungfrau [17], and a discussion of their parameters will be elaborated later. The maximum and minimum achievable design parameters, within this range of source-to-crystal distances, are summarised in table 1 for HAPG crystals operated in first order reflection. In general the dispersion for this setup is between 10.7 and 18.3 eV/mm on the detector plane.

The dispersion in this geometry is very close to linear and may be expressed simply in terms of the $2d$ spacing, radius-of-curvature R, diffraction order n (in our case 1), Planck's constant h, speed of light c, and Bragg angle θ:

$$\frac{dE}{dx} = hc\frac{n}{2d}\frac{\cos\theta}{2R},\tag{2.1}$$

for displacements dx along the detector plane. Considering small deviations $\delta\theta$ from a central Bragg angle θ_B, the deviation from linearity for $1°$ changes in Bragg angle (typical for this setup) is 0.4%.

Furthermore, the effect of mosaic focusing must be considered. In figure 1c, we show a not-to-scale model of mosaic focusing. In general, for a perfect crystal, the desired crystal reflection plane has its normal aligned uniformly throughout the crystal and aligned at some angle to the crystal's surface, depending on its cut, allowing incoming rays to reflect at the Bragg angle to the reflection's normal. However, for a mosaic crystal, the crystal is formed of crystallites with some

mosaic spread, or mosaicity as described above, meaning that the normal vectors of the crystallites are inclined by some range of angle ω to the average reflection normal. Consequently, rays that differ from the central Bragg angle by this mosaic spread, are also reflected from the crystal and are focused onto the detector. This has the effect of increasing the reflectivity of the crystal as a larger area reflects a monochromatic beam onto the detector. The length of the crystal along the dispersive axis that would reflect a monochromatic beam at a Bragg angle θ with mosaicity ω is:

$$\Delta x = \frac{R}{\sin^2(\theta)} 2\omega.$$

For an extremal configuration with an $R = 50$ mm HAPG crystal with mosaicity $\omega = 0.14°$ and at a central Bragg angle of 7° (photon energy $E_C = 14.9$ keV), the reflecting length is $\Delta x = 16.5$ mm. Even in this configuration, the crystal is large enough to fully reflect and focus all rays onto the detector, although this particular configuration would suffer more from depth broadening. A Jungfrau detector has a rectangular chip with a long edge of length ~ 80 mm and therefore only captures rays that are reflected from the central 40 mm of the 80 mm long crystal. The accepted range of Bragg angles (due to the long source-crystal distance) differ by $\sim \pm 0.2°$ and consequently approximately 11.8 mm of the crystal at each end is not used. This also means that the crystal does not need to be aligned along the cylinder axis to better than ~ 10 mm for all HAPG configurations. Note that for a HOPG crystal the mosaicity is approximately three times larger and therefore the area used for mosaic focusing is also three times larger. Using a HOPG crystal could lead to edge effects, whereby at the extremities of the spectral window the reflectivity might drop because the reflecting area is cut off at the end of the crystal. This could slightly reduce the usable spectral range if the relative reflectivity of spectral components at the extremities matter, and instead it may be preferable to use a higher order reflection instead. Edge effects are not expected to be a limitation for HAPG in this geometry: an extremal Δx of 40 mm would require a photon energy of ~ 24 keV in first order reflection.

3 Technical design

The spectrometer incorporates many improvements from previous designs [18] and is designed to be interchangeable with a range of different cylindrically-curved crystals. Two radii-of-curvature — 50 mm and 80 mm — are chosen, whilst meeting the constraints of a 200–400 mm source-crystal distance, to cover as wide a range of photon energies as possible: from 5–15 keV as detailed in table 1. Furthermore, in the range 7.6–9.4 keV both crystals may be used interchangeably depending on desired resolution, spectral window, distance to the source, collection solid-angle and consequent obstruction of other solid angles around the interaction point. The crystal arm has a length of 500 mm and is light-weight and manually adjustable before the experiment. The entire setup around the crystal is designed to be as unobtrusive as possible and to cover a minimal solid angle around the crystal, in order to allow its use with other diagnostics at close range. In other words, the crystal is suspended free from a protective housing and a PMMA shield can be added for plasma experiments with an expected debris spread. The crystal's width is reduced to 30 mm to minimise k-vector blurring and focal aberrations without detriment to its collection efficiency [9].

The detector mounting can be exchanged to accept either an ePix100 detector, or Jungfrau detector (in an airbox housing for use in vacuum) and incorporates a light-tight cap over the sensor
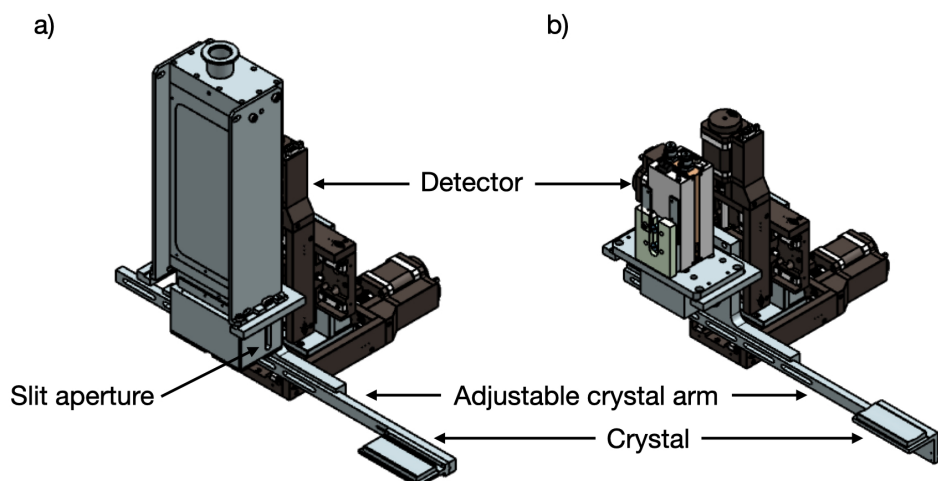
Figure 2. Drawing of Spectrometer design shown in two configurations with key components labelled. In a) a Jungfrau detector and $R = 80$ mm crystal are mounted. In b) an ePix100 detector and $R = 50$ mm crystal are mounted. The crystal arm has length 500 mm and is manually adjustable. Note that the $R = 50$ mm crystal in b) is mounted to a 30 mm high bracket which allows the same setup to be used interchangeably for different crystal R. The bracket holding the detector is designed such that it can be used with either a Jungfrau detector, or ePix100 detector with an adapter plate. The whole setup is motorised in three axes.

Table 2. Comparison of detectors.

Name	Pixel size (µm)	No. of pixels (adim.)	Detection area (mm^2)	Noise (eV)	Frame rate (Hz)	Dynamic Range (photons per pixel)
ePix100	50	704×768	35×38	< 280	120	10^2 8 keV
Jungfrau	75	512×1024	38.55×77.25	< 450	2400	10^4 12 keV

with a wide slit aperture to accept rays reflected from the crystal, attenuated with black kapton to block optical light (other attenuating foils, depending on background or source brightness, are available). A small light-shield (typically a thick Cu foil) can be attached to the detector holder to block direct light from the source onto the detector sensor. Some important parameters for these two detectors are compared in table 2, but both detectors ensure a dispersion ~ 1 eV/pixel depending on the exact setup. Note that the Jungfrau detector can be operated at > 100 kHz in burst mode and has its dynamic range spread over three gain stages. The entire spectrometer, detector, and crystal arm configuration is motorised in three axes allowing the setup to be fine-aligned in vacuum using x-rays. Any error in alignment of the crystal-to-detector distance may be compensated thus. This entire setup is made as light-weight as possible from Al parts, so that it can be mounted onto a curved-rail system, centred on the interaction point, allowing changes in scattering angle without breaking vacuum. A schematic of the design is shown in figure 2.

For each radius-of-curvature, two different HAPG coating thicknesses, 40 µm and 100 µm, deposited onto optical-quality glass substrates through contact bonding, are chosen in order to

further give the optimal trade-off in reflectivity and resolution. Thicker coatings, at thicknesses less than the absorption depth of the x-rays, have a higher reflectivity which is limited by photo-absorption losses and Bragg extinction [8]. However, whilst they are more reflective, they suffer from inferior resolution due to an increase in depth broadening, and are not the best choice if one strives for the highest possible resolution.

We can also consider the integrated efficiency for these two HAPG coatings which is the angular size in the non-dispersive direction (in rad) multiplied by the integrated reflectivity (also in rad) in the dispersive direction to give a solid angle Ω. First, the angular size of the 30 mm wide crystal in the non-dispersive direction is 150 mrad for $x = 200$ mm and 75 mrad for $x = 400$ mm. At 8.05 keV, for a 40 μm thick crystal [8], the integrated efficiency Ω is $1.0–2.0 \times 10^{-4}$ sr over this range of source-detector distances. For the thicker 100 μm crystal, $\Omega = 1.7–3.4 \times 10^{-4}$ sr. This enables, notwithstanding the detector efficiency, the calculation of expected photon numbers for an experimental setup. Typically, $8.0 – 27.1 \times 10^{-6}$ of all photons emitted isotropically into 4π will be collected by the crystal.

4 Spectrometer calibration measurements

Four HAPG crystals were commissioned in two separate experimental campaigns at the High Energy Density (HED) instrument of the European XFEL [19, 20]. In the first campaign, the two 50 mm crystals of different thicknesses were calibrated simultaneously using two independent spectrometer configurations. The XFEL beam was operated in SASE single-bunch mode at an FEL energy of 8882 ± 10 eV, with a repetition rate of 10 Hz. The energy delivered was 1.10 ± 0.14 mJ, or $7.7 \pm 1.0 \times 10^{11}$ photons-per-pulse measured upstream of the target using an X-ray Gas Monitor (XGM) [21, 22]. The x-ray pulses were weakly-focussed using beryllium compound refractive lenses (CRLs) 742 m upstream of the interaction point to a spot of size ~ 100 μm giving an emitting source of volume $\sim 5 \times 10^4$ μm^3. Emission from sandwich targets comprising layers of 2 μm thick iron, cobalt, and nickel were recorded on two spectrometers and used to align and calibrate them along the dispersive axis. The recorded spectra are shown in figure 3. The forward-scattering spectrometer was set to a near zero forward-scattering angle relative to the FEL beam, with its crystal just above the beam axis, and employed a Jungfrau detector and HAPG crystal with a thickness of 40 μm. Its spectrum is shown in figure 3a averaged over 184 shots and was centred at an energy of 7000 eV with a spectral window of $\Delta E = 1359$ eV. The backward-scattering spectrometer was set to a near backward-scattering angle relative to the FEL beam, again with its crystal just above the beam axis, and employed an ePix100 detector and HAPG crystal with a thickness of 100 μm. Its spectrum, for the sandwich target, is shown in figure 3b averaged over 100 shots and was centred at an energy of ~8575 eV with a spectral window of $\Delta E = 677$ eV. Both images in figure 3 were taken contemporaneously. Additionally, the backward-scattering spectrometer used a 2 μm thick copper foil for calibration as described below.

Since in this configuration the two spectrometers observe different spectral windows they were calibrated independently. The forward spectrometer was calibrated with the five lines of Fe Kα, Fe Kβ, Co Kα, Co Kβ, and Ni Kα. The backward spectrometer was calibrated using the Ni Kβ and Cu Kα line (not shown) by tuning the FEL energy up to 9000 eV, above the Cu K-edge. The dispersion was linear as expected and found to be 1.32 eV/pixel for the forward spectrometer and 0.88 eV/pixel for the backward matching designed values and are shown in black and grey in figure 5.
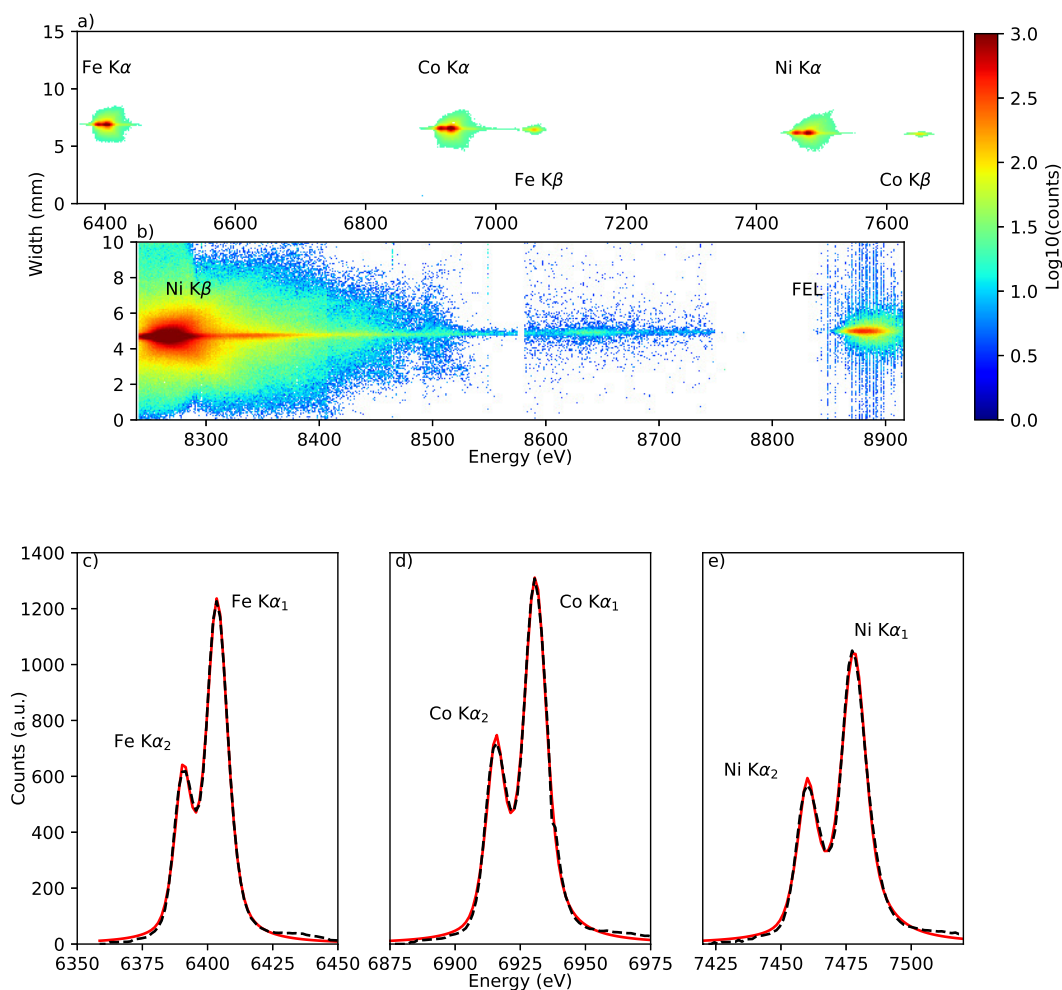
Figure 3. Spectra taken with two spectrometers employing $R = 50\,\mathrm{mm}$ HAPG crystals. Above a) shows the forward-scattering spectrometer with emission lines from Fe, Co, and Ni. In b) we show the backward-scattering spectrometer with Ni Kβ and the FEL labelled. The colour scale is logarithmic and corresponds to both figures — white corresponds to zero counts. Below: lineouts (black dashed) from the image shown in a). Left c) shows the Fe Kα doublet fitted (in red) with the sum of two Pseudovoigt profiles. Similarly in d) (centre) and in e) (right) the Co Kα and Ni Kα doublets are shown fitted (in red).

Another important metric is the spectrometer's instrument function. This arises as the combination of various sources of additional broadening of each photon energy due to a combination of several effects such as source-size, pixel-size, charge sharing effects, focal aberrations, mosaicity, and depth broadening from the crystal thickness. The forward spectrometer with the $40\,\mu\mathrm{m}$ thick crystal was found to have an excellent instrument function as shown in figure 3c–e. All Kα doublets are resolved and are fitted with the sum of two Pseudovoigt profiles (following eqs. 6-10 of ref. [23]). Their FWHM are summarised in table 3 with measured values [24] in parentheses and imply an instrumental broadening of $\sim 5 - 8\,\mathrm{eV}$, in perfect agreement with previously published

Table 3. Fitted FWHM (tabulated/reference values in parentheses [24])

	Energy Kα_1 (eV)	FWHM Kα_1 (eV)	FWHM Kα_2 (eV)
Fe	6404	9.89 (2.55)	7.70 (3.14)
Co	6930	10.62 (2.33)	8.63 (3.18)
Ni	7478	11.72 (2.24)	8.98 (3.41)

values [8]. Similarly, the backward spectrometer using the thicker 100 μm HAPG crystal shows a Ni Kβ line with FWHM of 22.8 eV (measured value [24] 5.40 eV) and an elastically scattered FEL with a FWHM of 25.0 eV, giving an instrumental broadening of $\sim$ 17 eV. This matches previously published values [8] measured using a slit $\sim$ 100 − 200 μm, thus confirming our larger emitting volume and corresponding increase in source broadening. Furthermore, the ratio of instrument functions is as expected for the increase in depth broadening with a 2.5 times thicker crystal.

The two 80 mm crystals of different thicknesses were calibrated in a second experiment at the HED instrument. This time the pulse train was also operated in SASE mode at an FEL energy of 5992 ± 10 eV, again with one bunch-per-train at 10 Hz. The pulses were then attenuated with solid attenuators to $\sim$ 1% resulting in 23 ± 5 μJ or 2.4 ± 0.5 × 10^{10} photons-per-pulse measured upstream of the target using an X-ray Gas Monitor (XGM) [21, 22], before the final focussing optics. The x-ray pulses were focussed using beryllium compound refractive lenses (CRLs) 9 m upstream of the interaction point to a spot of size $\sim$ 10 μm giving an emitting source of volume $\sim$ 400 μm^3. Characteristic K-shell emission from 5 μm thick chromium foils were recorded on two spectrometers, as well as elastically-scattered incident FEL photons, and used to align and calibrate them along the dispersive axis. The recorded spectra are shown in figure 4. The forward-scattering spectrometer was set to an angle of $\sim$ 18° relative to the FEL beam and employed an ePix100 detector and HAPG crystal with a thickness of 100 μm. Its spectrum is shown in figure 4a and was centred at an energy of 6050 eV with a spectral window of $\Delta E = 448$ eV. The backward-scattering spectrometer was set to an angle of $\sim$ 155° relative to the FEL beam and employed a Jungfrau detector and HAPG crystal with a thickness of 40 μm. Its spectrum is shown in figure 4b and was centred at an energy of 5650 eV with a spectral window of $\Delta E = 839$ eV.

The two sets of images were taken simultaneously from an average of 1016 shots and allow both detectors to be calibrated. First, the backward spectrometer was calibrated using the Cr Kα and Cr Kβ emission lines. This yields the FEL energy from the recorded elastically-scattered photons on the backward spectrometer, which, with the Cr Kβ line, allowed the forward spectrometer to be calibrated. The dispersion was found to be 0.82 eV/pixel for the forward spectrometer and 0.58 eV/pixel for the backward matching designed values and are shown in blue and light-blue in figure 5.

The backward spectrometer with the 40 μm thick crystal was found to have an excellent instrument function, due to the combination of a large bending radius and thin HAPG crystal, as shown in figure 4c-d. The Cr Kα lines were well-separated and found to be well-approximated by the sum of two Pseudovoigt profiles, as described above, with Full-Width-Half-Maximum (FWHM) of Kα_1 = 3.89 eV and Kα_2 = 4.93 eV. This compares well to their measured values [24] of Kα_1 = 1.88 eV and Kα_2 = 2.52 eV and implies an instrument function of ~2 eV, assuming the broadening contributions combine linearly. The Cr Kβ line for this spectrometer had a width Cr Kβ = 5.21 eV (measured value 2.53 eV [24]), also in good agreement. The forward spectrometer
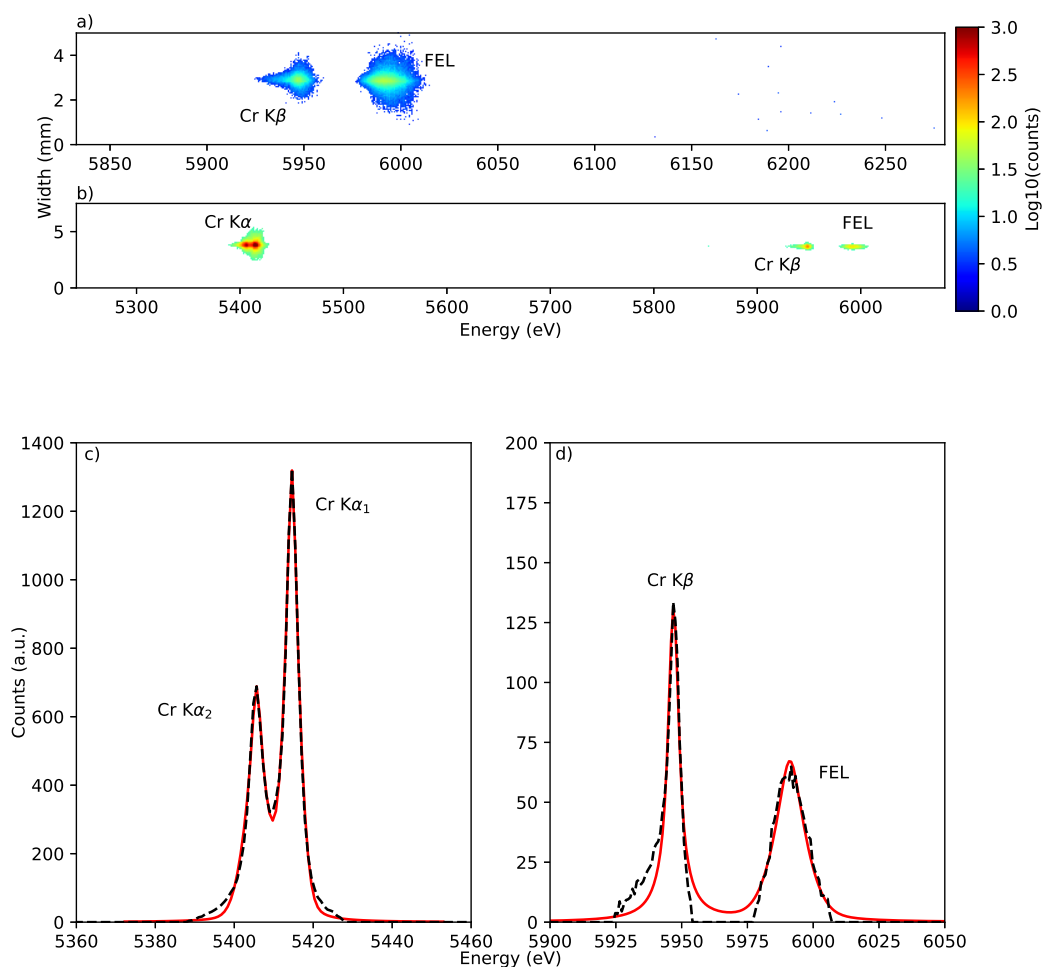
Figure 4. Spectra taken with two spectrometers employing R = 80mm HAPG crystals. Above a) shows the forward-scattering spectrometer with emission from Cr $K\beta$ and the FEL labelled. In b) we show the backward-scattering spectrometer with additionally Cr $K\alpha$ labelled. The colour scale is logarithmic and corresponds to both figures. Below: lineouts (black dashed) from the image shown in b). Left c) shows the Cr $K\alpha$ doublet fitted (in red) with the sum of two Pseudovoigt profiles. In d) right the Cr $K\beta$ and neighbouring elastically-scattered FEL profile are shown fitted (in red) to the sum of two Pseudovoigt profiles. The FEL profile is found to be approximately Gaussian as expected. The drop between the two line profiles in d) is due to the noise treatment of the detector: counts below one standard deviation of the noise are set to zero. Asymmetry is visible in the Cr $K\beta$ originating from a $K\beta'$ component due to different configurations of spectator electrons in the d-shell [25, 26].

using the thicker $100\,\mu$m HAPG crystal shows a Cr $K\beta$ with a FWHM of 7.56 eV, implying a ~5 eV broadening. Note that the ratio of the instrument functions is as expected for the increase in depth broadening with a 2.5 times thicker crystal, given that the crystal line-of-sight thicknesses (at $\theta_B \sim 18°$) are less than the attenuation length (400 μm at 6 keV). The elastically-scattered SASE spectrum of the FEL had a measured FWHM of 12.8 eV on the backward spectrometer and 15.4 eV on the forward spectrometer. The measured parameters for all four crystals are summarised in table 4.
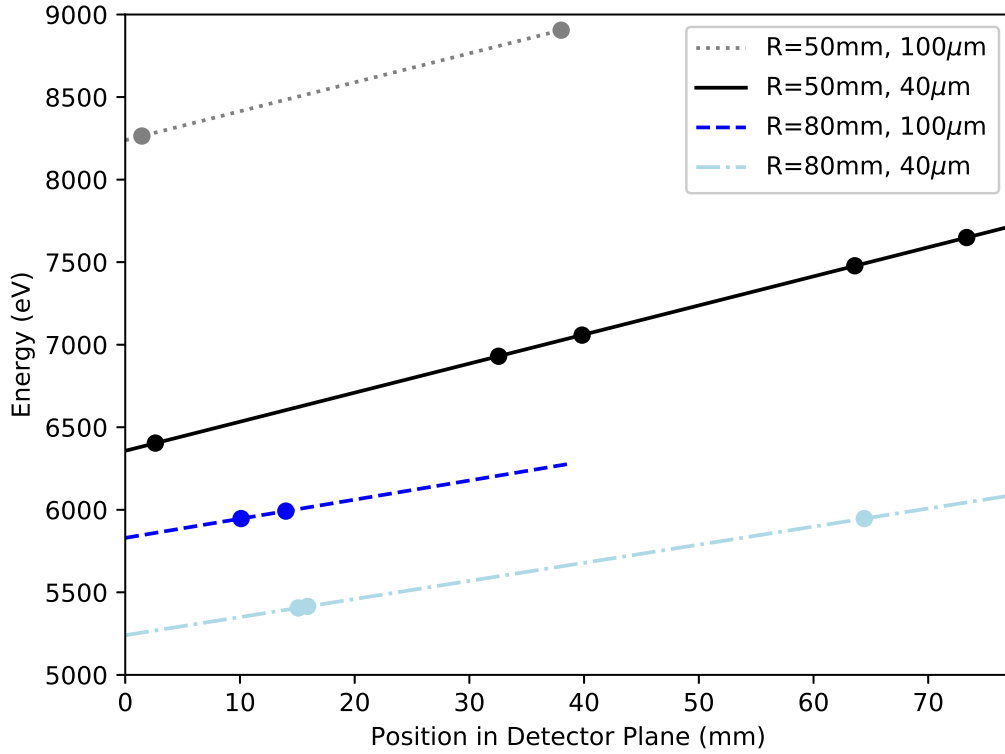
Figure 5. Dispersion of all spectrometer configurations as a function of position along the detector plane labelled according to crystal radius-of-curvature and thickness. Note, the dispersion steepens at higher photon energies due to the correspondingly smaller Bragg angle and radius-of-curvature of eq. (2.1). Shown in blue dashed is the forward-scattering spectrometer of figure 4a and light-blue dot-dashed is the backward-scattering spectrometer of figure 4b. Black is the forward-scattering spectrometer of figure 3a and grey dotted is the backward-scattering spectrometer of figure 3b. Circular points are the lines used to fit the dispersion as described in the text.

Table 4. Measured parameters for all four crystals. Radius-of-curvature (R), thickness (t), central energy (E_C), spectral window (ΔE), dispersion (dE/dx), instrumental broadening (IF), and Resolving power (RP = E_C/IF).

R (mm)	t (μm)	E_C (eV)	ΔE (eV)	dE/dx (eV/pixel)	IF (eV)	RP (adim.)
80	40	5650	839	0.58	2	2.8×10^3
80	100	6050	448	0.82	5	1.2×10^3
50	40	7000	1359	1.33	5–8	0.9–1.4×10^3
50	100	8575	677	0.88	17	0.5×10^3

As mentioned earlier there is often a trade off in crystal-to-detector distance, radius-of-curvature, and spectral window, and in general, due to the smaller Bragg angle on the crystal, larger distances correspond to higher photon energies. As an example of this, in the experiment with the $R = 50$ mm crystals, the forward spectrometer of figure 3a was operated at a shorter than de-
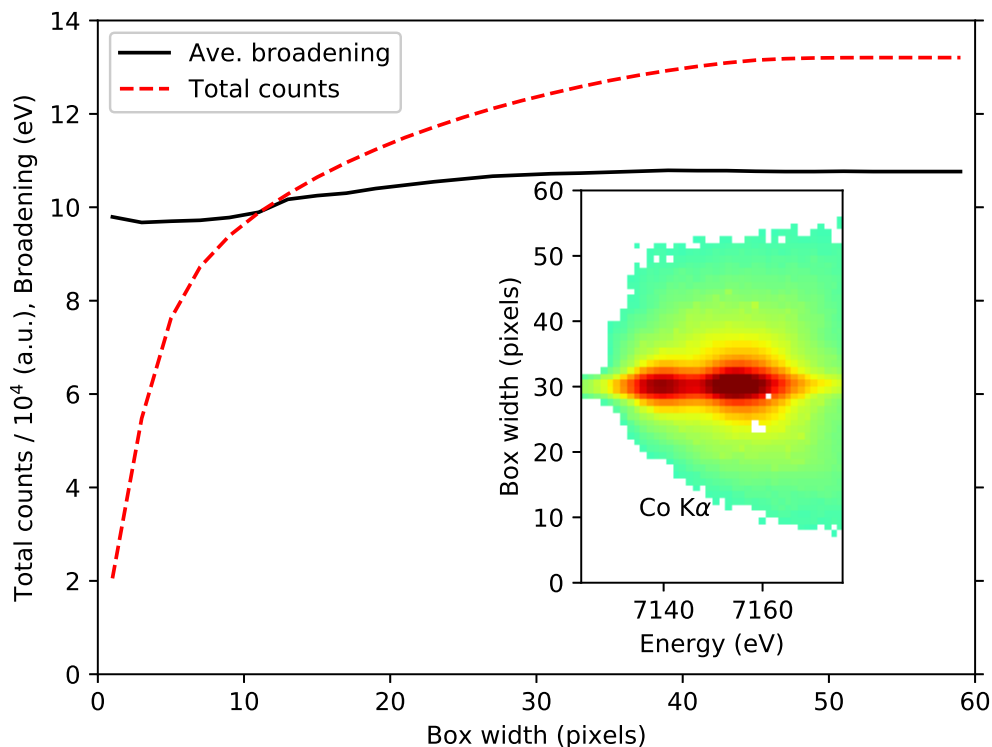
Figure 6. Fitted average broadening (black) of the two lines in the Co Kα doublet and total integrated counts (red dashed) as the box width along the non-dispersive direction is varied from 1 to 60 (full height of inset). The Co Kα doublet is shown in the inset with the same logarithmic colour-scale as figure 3a). The optimum box width is found to be less than three pixels and corresponds to that shown in figure 3d.

signed crystal-to-detector distance of 174 mm in order to move the spectral window lower in energy to include the Fe Kα. A Jungfrau detector was used to maximise the spectral window. The desired central photon energy of 7000 eV could have been accommodated with the $R = 80$ mm crystal at a distance within the designed envelope (200–400 mm), but then ΔE would have been ~ 800 eV as seen in the experiment of figure 4b — too small for this experiment which required $\Delta E > 1000$ eV in order to observe emission from Fe, Co, and Ni without changes in spectrometer setup.

In calculating the instrument function, a box of width three pixels was taken around the central line focus of the cylindrically bent crystal. The effect of bounding box size is investigated in figure 6 on the total counts in the box (related to the total number of photons) and the average of the fitted widths of the two line profiles in the Co Kα doublet of figure 3d. The selected region-of-interest (ROI) of the detector is shown as an inset of figure 6. As expected, increasing the box size includes more of the photons which are scattered outside of the central line focus due to the crystal's mosaicity. This scattering also slightly increases the broadening of the line as depending on the orientation of the mosaic crystallites the photons may be scattered both "up" in energy as well as "down", relative to the dispersion along the central line focus. Since the width of the crystal is reduced to 30 mm, we do not observe a pronounced X-shape aberration [7, 8]. Nevertheless, an

optimum is found here for a box of size three pixels since this box captures 42% of the total photons recorded on the detector for this line doublet with no increase in broadening from aberrations.

5 Conclusions

We have successfully designed, built, and demonstrated the spectroscopy capabilities of the HED instrument using highly-reflective cylindrically-bent HAPG crystals operated in von Hámos geometry. The spectrometer fulfills all the requirements of the HED chamber, has a slim design, and is applicable to a range of scientific requirements in terms of resolution, efficiency and spectral window. The spectrometer performs as designed over the energy range of 5–9 keV and furthermore the instrument function and resolving power for a configuration using a crystal with radius-of-curvature of 50 mm is as previously reported [8]. Using crystals with a larger radius-of-curvature (80 mm) gives a corresponding improvement in instrument function down to 2 eV at 5–6 keV. This would allow features to be resolved in the future with an unprecedented precision using HAPG crystals, especially when operated in conjunction with an x-ray beam that has undergone self-seeding to reduce its bandwidth down to ~ 1 eV, or indeed used in conjunction with a monochromator (in preparation).

References

[1] D. Kraus, B. Bachmann, B. Barbrel, R.W. Falcone, L.B. Fletcher, S. Frydrych et al., *Characterizing the ionization potential depression in dense carbon plasmas with high-precision spectrally resolved x-ray scattering*, *Plasma Phys. Contr. Fusion* **61** (2019) 014015.

[2] T.R. Preston, K. Appel, E. Brambrink, B. Chen, L.B. Fletcher, C. Fortmann-Grote et al., *Measurements of the momentum-dependence of plasmonic excitations in matter around 1 Mbar using an X-ray free electron laser*, *Appl. Phys. Lett.* **114** (2019) 014101.

[3] H.J. Lee, P. Neumayer, J. Castor, T. Döppner, R.W. Falcone, C. Fortmann et al., *X-Ray Thomson-Scattering Measurements of Density and Temperature in Shock-Compressed Beryllium*, *Phys. Rev. Lett.* **102** (2009) 115001.

[4] J.K. Cooper, S. Gul, F.M. Toma, L. Chen, Y.-S. Liu, J. Guo et al., *Indirect Bandgap and Optical Properties of Monoclinic Bismuth Vanadate*, *J. Phys. Chem. C* **119** (2015) 2969.

[5] P. Sperling, S. Rosmej, R. Bredow, L.B. Fletcher, E. Galtier, E.J. Gamboa et al., *Electrical conductivity calculations in isochorically heated warm dense aluminum*, *J. Phys. B* **50** (2017) 134002.

[6] L. v. Hámos, *Röntgenspektroskopie und Abbildung mittels gekrümmter Kristallreflektoren II. Beschreibung eines fokussierenden Spektrographen mit punktgetreuer Spaltabbildung*, *Ann. Phys.* **411** (1934) 252.

[7] U. Zastrau, C.R.D. Brown, T. Döppner, S.H. Glenzer, G. Gregori, H.J. Lee et al., *Focal aberrations of large-aperture HOPG von-Hàmos x-ray spectrometers*, 2012 *JINST* **7** P09015.

[8] U. Zastrau, A. Woldegeorgis, E. Förster, R. Loetzsch, H. Marschner and I. Uschmann, *Characterization of strongly-bent HAPG crystals for von-Hámos x-ray spectrographs*, 2013 *JINST* **8** P10006.

[9] U. Zastrau, L.B. Fletcher, E. Förster, E.C. Galtier, E. Gamboa, S.H. Glenzer et al., *Bent crystal spectrometer for both frequency and wavenumber resolved x-ray scattering at a seeded free-electron laser*, *Rev. Sci. Instrum.* **85** (2014) 093106.

[10] J. Szlachetko, M. Nachtegaal, E. de Boni, M. Willimann, O. Safonova, J. Sa et al., *A von Hamos x-ray spectrometer based on a segmented-type diffraction crystal for single-shot x-ray emission spectroscopy and time-resolved resonant inelastic x-ray scattering studies*, *Rev. Sci. Instrum.* **83** (2012) 103105.

[11] S. Glenzer and R. Redmer, *X-ray Thomson scattering in high energy density plasmas*, *Rev. Mod. Phys.* **81** (2009) 1625.

[12] P. Neumayer, C. Fortmann, T. Döppner, P. Davis, R.W. Falcone, A.L. Kritcher et al., *Plasmons in Strongly Coupled Shock-Compressed Matter*, *Phys. Rev. Lett.* **105** (2010) 075003.

[13] L.B. Fletcher, E. Galtier, P. Heimann, H.J. Lee, B. Nagler, J. Welch et al., *Plasmon measurements with a seeded x-ray laser*, 2013 *JINST* **8** C11014.

[14] B.B. Witte, L.B. Fletcher, E. Galtier, E. Gamboa, H.J. Lee, U. Zastrau et al., *Warm Dense Matter Demonstrating Non-Drude Conductivity from Observations of Nonlinear Plasmon Damping*, *Phys. Rev. Lett.* **118** (2017) 225001.

[15] H. Legall, H. Stiel, M. Schnürer, M. Pagels, B. Kanngießer, M. Müller et al., *An efficient X-ray spectrometer based on thin mosaic crystal films and its application in various fields of X-ray spectroscopy*, *J. Appl. Cryst.* **42** (2009) 572.

[16] K. Nishimura, G. Blaj, P. Caragiulo, G. Carini, A. Dragone, G. Haller et al., *Design and performance of the ePix camera system*, *AIP Conf. Proc.* **1741** (2016) 040047.

[17] A. Mozzanica, A. Bergamaschi, M. Brueckner, S. Cartier, R. Dinapoli, D. Greiffenberg et al., *Characterization results of the JUNGFRAU full scale readout ASIC*, 2016 *JINST* **11** C02047.

[18] B. Nagler, B. Arnold, G. Bouchard, R.F. Boyce, R.M. Boyce, A. Callen et al., *The Matter in Extreme Conditions instrument at the Linac Coherent Light Source*, *J. Synchrot. Radiat.* **22** (2015) 520.

[19] W. Decking, S. Abeghyan, P. Abramian, A. Abramsky, A. Aguirre, C. Albrecht et al., *A MHz-repetition-rate hard X-ray free-electron laser driven by a superconducting linear accelerator*, *Nature Phot.* **14** (2020) 391.

[20] T. Tschentscher, C. Bressler, J. Grünert, A. Madsen, A. Mancuso, M. Meyer et al., *Photon Beam Transport and Scientific Instruments at the European XFEL*, *Appl. Sci.* **7** (2017) 592.

[21] J. Grünert, M.P. Carbonell, F. Dietrich, T. Falk, W. Freund, A. Koch et al., *X-ray photon diagnostics at the European XFEL*, *J. Synchrot. Radiat.* **26** (2019) 1422.

[22] T. Maltezopoulos, F. Dietrich, W. Freund, U.F. Jastrow, A. Koch, J. Laksman et al., *Operation of X-ray gas monitors at the European XFEL*, *J. Synchrot. Radiat.* **26** (2019) 1045.

[23] T. Ida, M. Ando and H. Toraya, *Extended pseudo-Voigt function for approximating the Voigt profile*, *J. Appl. Cryst.* **33** (2000) 1311.

[24] G. Hölzer, M. Fritsch, M. Deutsch, J. Härtwig and E. Förster, *$k\alpha_{1,2}$ and $k\beta_{1,3}$ x-ray emission lines of the 3d transition metals*, *Phys. Rev. A* **56** (1997) 4554.

[25] D. Anagnostopoulos, *X-ray emission spectroscopy optimization for chemical speciation in laboratory*, *Spectrochim. Acta B* **148** (2018) 83.

[26] S. Fazinić, L. Mandić, M. Kavčič and I. Božičević, *Parametrization of Kβ" and $K\beta_{2,5}$ X-ray contributions in Kβ spectra of 3d transition metal compounds*, *J. Anal. Atom. Spectrom.* **26** (2011) 2467.